Differential thermal analysis to assist the design of corrosion-resistant high entropy alloys for laser powder bed fusion

SEIDOU Abdul Herrim[1,a] *, BLONDIAU Catherine[1,b], DEDRY Olivier[1,c],
OÑATE Angelo[2,d], TUNINETTI Víctor[3,e],
TCHOUFANG TCHUINDJANG Jérôme[1,f], and MERTENS Anne[1,g]

[1] Metallic Materials Science (MMS), A&M Dept, University of Liège, Liège, 4000, Belgium

[2]Dept of Materials Engineering, Universidad de Concepción, Edmundo Larenas 315, Concepción, Chile

[3]Dept of Mechanical Engineering, Universidad de La Frontera, Francisco Salazar 01145, Temuco, Chile

[a]ahb.seidou@uliege.be, [b]catherine.blondiau@student.uliege.be, [c]olivier.dedry@uliege.be,
[d]aonates@udec.cl, [e]Victor.tuninetti@ufrontera.cl, [f]j.tchuindjang@uliege.be,
[g]anne.mertens@uliege.be

Keywords: High Entropy Alloys, Alloy Design, DTA, Solidification Path, Microstructure

Abstract. In this study, Al, Cr, Fe, Mn, and Ni are selected and pure elemental powders were used to prepare several medium entropy alloys (MEAs) and high entropy alloys (HEAs). Differential Thermal Analysis (DTA) is used as a tool for pre-screening of the compositions suitable to design corrosion-resistant alloys for Laser Powder Bed Fusion (LPBF). The advantage of DTA lies in the precise temperature control and in the small quantity of powder necessary to perform the test in near-equilibrium conditions. The powder mixtures were heated up to 1550°C, fully melted, and then cooled down to room temperature at 5°C/min. The results of DTA are used as reference to understand the complex microstructures obtained using LPBF. Microstructure analysis of DTA samples by combining Optical Microscopy (OM) and Scanning Electron Microscopy (SEM) helped to confirm the phase prediction theories. Most of the samples showed a heterogeneous structure with Ni-Al rich B2 phase, Fe-Cr rich BCC and FCC phases. The spinodal decomposition of the BCC phase was also observed in the equimolar AlCrFeMnNi sample. The Valence Electron Concentration (VEC) theory was verified and the partitioning of the elements between the phases was investigated.

Introduction

Additive manufacturing (AM) technologies, such as Laser Powder Bed Fusion (LPBF), allow the creation of intricate parts with features that pose challenges for conventional methods. Notably, LPBF has revolutionized the manufacturing of components traditionally crafted through injection molding or die-casting, marking a departure from conventional approaches [1,2]. In comparison to standard casting and forging techniques, the melt-pool generated in LPBF is submitted to exceptionally high cooling rates in a range from 10^3 to 10^6 K/s [3]. This rapid cooling induces an out-of-equilibrium solidification, promoting grain refinement and potentially leading to the formation of novel sub-crystal or amorphous phases [4]. LPBF offers a better design flexibility and functional optimization of high-value products at small production volumes, which are not feasible through traditional manufacturing processes [5]. LPBF processes often operate with fixed parameters for specific applications, limiting the responsive control. The choice of input materials and printing parameters can lead to variations in the properties of the final components. A poor powder quality can cause defects such as pores, cracks, inclusions, residual stresses, suboptimal roughness. Therefore, understanding the intricate relationships between material properties,

processing performance, and end component properties is necessary to develop alloys that fulfill the requirements [6,7].

High entropy alloys (HEAs) were defined originally as alloys that contain more than five principal elements with the concentration of each between 5% and 35%. This concept of HEAs has been lately extended to alloys with four principal elements [8,9]. Due to the high mixing entropy effect, the crystal lattice structure of most HEAs tends to be either body-centered cubic (BCC) or face-centered cubic (FCC). BCC-structured HEAs typically exhibit high strength but low ductility, whereas FCC-structured HEAs showcase high ductility, high wear, and corrosion resistance, with relatively low strength [10,11]. Consequently, a judicious selection of alloying elements is vital to achieve the required properties in HEAs.

Conventional casting, with cooling rates between 10 and 20 K/s, usually causes significant phase separation during the fabrication process of HEAs, where a post-treatment process is usually required to further adjust the microstructure for desired properties [10]. The rapid solidification of LPBF can restrict compositional segregation and intermetallics formation in the as-built parts, contributing to the strengthening effect through grain refinement [12].

In recent efforts to predict phases in HEAs, theories have been developed based on thermodynamic and structural parameters, including entropy of mixing (ΔS_{mix}), atomic size differences (δ), melting points (T_m), enthalpy of mixing (ΔH_{mix}), valence electron concentration (VEC), and Ω that represents the scale ratio of ΔS_{mix} to ΔH_{mix}. These parameters play crucial roles in determining the stability and composition of solid-solution phases in HEA systems [8,13]. The electron concentration is defined as the average number of itinerant electrons per atom (e/a) and the VEC encompasses all electrons, including the d-electrons accommodated in the valence band [14,15]. For a multi-component alloy, both e/a and VEC can be mathematically expressed by Eq. 1 and Eq. 2:

$$e/a = \sum_{i=1}^{n} c_i (e/a)_i \tag{1}$$

$$VEC = \sum_{i=1}^{n} c_i (VEC)_i \tag{2}$$

Here, c_i represents the concentration of the individual element in the alloy, $(e/a)_i$ and $(VEC)_i$ denote the e/a and VEC for the respective element. A stable, solid-solution phase forms in an HEA system when two parameters meet the conditions $\Omega > 1.1$ and $\delta < 6.6\%$ [14,16]. Specifically, when VEC > 8, FCC solid-solution phase is established. In the range of $6.87 \leq VEC < 8$, both FCC and BCC phases coexist. However, when VEC < 6.87, only a single BCC phase is observed [11].

Regarding the corrosion resistance properties, alloys with higher Al and lower Cr contents tend to develop porous oxide films on the surface, failing to provide effective barriers against Cl⁻ permeation. Moreover, the high Al content promotes the growth of the BCC phase, characterized by enrichment in Al and depletion of Cr, leading to increased elemental segregation. This, in turn, influences the corrosion behavior, with the Cr-depleted BCC phase demonstrating weaker corrosion resistance compared to the FCC phase [17]. The control of the microstructure is thus fundamental in developing materials with specific properties.

Thermal analysis methods may be used to investigate the thermodynamic phenomena during the phase transformations. Differential Thermal Analysis (DTA) in particular employs the temperature difference between an inert reference sample and the test sample, during a thermal ramp conducted in a furnace with a fixed cooling rate. However, commercial DTA equipment faces limitations, notably in sample size, hindering adequate nucleation statistics. Consequently, while DTA has been employed in solidification experiments, its use in metal solidification studies is less frequent due to these inherent challenges [18,19]. However, in order to avoid the use of large amount of material to investigate the thermodynamic phenomena and perform preliminary microstructural characterization, DTA represents a rapid and cost-effective solution. Due to the small amount of material needed for DTA, mixture of powders represents an efficient choice to

prepare several alloys compositions. For HEAs design through AM technologies, this method is useful to select the elements by highlighting their influence on the microstructure and on the near-equilibrium solidification phenomena that will serve as reference to understand the as-built AM microstructure.

Materials and methods

Elemental powders, supplied by abcr GmbH (Germany), were employed in the fabrication of the test samples. Multiple mixtures were prepared manually, delineating two distinct groups: the CrFeMnNi-based medium entropy alloys (MEAs) and the AlCrFeMnNi-based HEAs. The nominal composition of the powder blends is outlined in Table 1 and Table 2.

Thermal analysis was conducted using the NETZSCH STA 449C Jupiter DTA. Approximately 700 mg of powder mixture were used for each DTA test. To facilitate near-equilibrium solidification and enable cross comparisons of the results, the heating and cooling rates were consistently maintained at 5°C/min. The samples underwent heating up to 1550°C within Al_2O_3 crucibles in an argon gas-purged chamber to minimize oxygen levels. An essential baseline measurement involved an empty crucible subjected to the same temperature profile, eliminating any artificial signals originating from the sample holder.

Table 1. Compositions and thermodynamic parameters of CrFeMnNi-based MEAs.

% at.	Cr	Fe	Mn	Ni	δ	ΔH_{mix}	ΔS_{mix}	Ω	VEC
CrFeMnNi	25	25	25	25	3.57	-4.00	11.53	5.21	7.75
Cr_2Fe_2MnNi	33.33	33.33	16.67	16.67	3.10	-2.88	11.05	7.16	7.50
$CrFe_2MnNi_2$	16.67	33.33	16.67	33.33	3.12	-4.22	11.05	4.70	8.17

Table 2. Compositions and thermodynamic parameters of AlCrFeMnNi-based HEAs.

% at.	Al	Cr	Fe	Mn	Ni	δ	ΔH_{mix}	ΔS_{mix}	Ω	VEC
AlCrFeMnNi	20	20	20	20	20	5.82	-12.48	13.38	1.75	6.80
$AlCrFe_2MnNi_2$	14.29	14.29	28.57	14.29	28.57	5.41	-10.86	12.89	1.98	7.43
$AlCrFe_2Ni_2$	16.67	16.67	33.33	-	33.33	5.47	-11.11	13.37	2.07	7.50

The samples underwent polishing for microstructural observation under an optical microscope (OM) or a scanning electron microscope (SEM) Tescan Clara Ultra-High Resolution UHR. Cr_2Fe_2MnNi and CrFeMnNi samples are etched with 3% Nital to improve the detection of phases during quantification with Stream analysis software. Additionally, semi-quantitative energy dispersive X-ray spectroscopy (EDX) point and line scan analyses were performed across notable microstructural features. Phase and crystallographic information were obtained through electron backscatter diffraction (EBSD).

Results

The DTA cooling curves of CrFeMnNi-based MEAs are shown in Fig. 1a. Reactions that occur during the cooling are characterized by exothermic peaks. For clarity, the derivative curves used

to determine the corresponding peak temperatures, but also to set both the beginning and the end of any given phase transformation, as reported in previous works, are not shown in this figure [20,21].

The $CrFe_2MnNi_2$ curve is characterized by a single peak at 1350°C (Fig. 1a). The OM and SEM micrographs, combined with EDX measurements, reveal the presence of one single FCC phase with composition close to the nominal composition of the alloy (Table 1). A single-phase structure is obtained, and the VEC value of 8.17 (Table 1) confirms the prediction theory. According to the same theory, CrFeMnNi and Cr_2Fe_2MnNi, that present respectively a VEC values of 7.75 and 7.50 (Table 1), should present a dual-phase structure associating FCC and BCC phases.
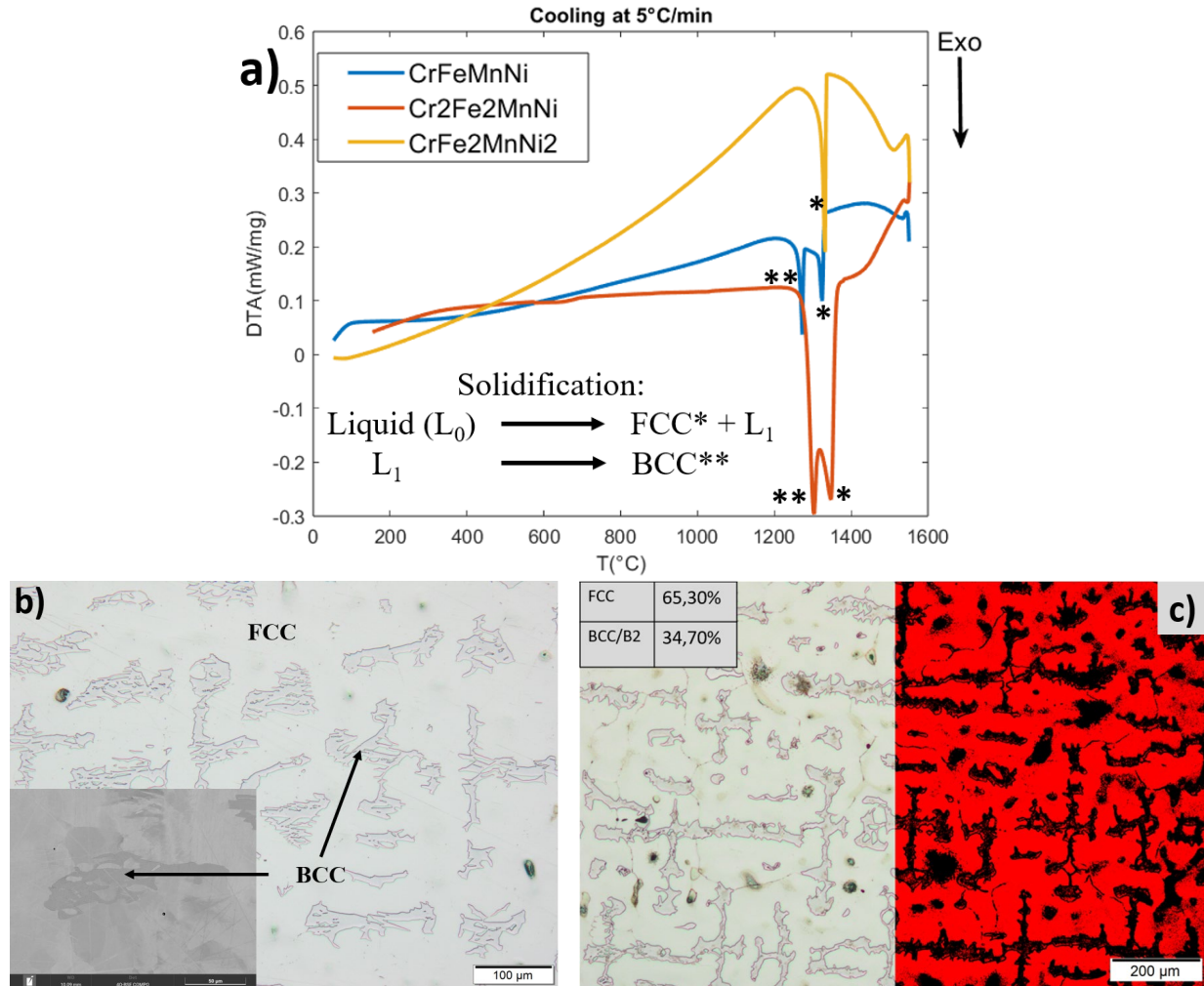

Fig. 1. (a) DTA cooling combined plots for alloys CrFeMnNi, Cr₂Fe₂MnNi and CrFe₂MnNi₂, (b) optical and scanning electron micrographs of alloy CrFeMnNi, (c) quantification of the phases in alloy CrFeMnNi using stream analysis.

Observing the micrographs of CrFeMnNi (Fig. 1b), two phases can be identified. The DTA cooling curve, in Fig. 1a, reveals two different peaks in a range of temperature between 1360°C and 1260°C (Fig. 1a). The first phase to form was the Fe-Cr rich FCC matrix, followed by the BCC phase that is rich in Mn and Ni (Table 3). The FCC phase forms due to the dendritic solidification. The remained liquid in the interdendritic region solidifies to form the BCC phase around 1300°C. CrFeMnNi and Cr_2Fe_2MnNi are very similar in terms of microstructure and distribution of elements between the phases (Table 4). The solidification temperature of Cr_2Fe_2MnNi is higher, in a range of temperature between 1380°C and 1280°C, as shown in Fig.

1a. The main difference lies in the volume fraction of the two phases. Using Stream analysis software on the optical micrographs, as shown in the left-hand side of Fig. 1c, the phases present in the microstructures were quantified. As an example of such analysis, the FCC matrix is highlighted in red on the right-hand side of Fig. 1c. In the Cr_2Fe_2MnNi sample, the percentage of FCC phase was 59.7% (40.3% of BCC). As Fe and Cr is increased, the percentage of BCC phase increases and the temperature at which the solidification starts is also increased, passing from 1360°C for the equimolar sample CrFeMnNi to 1380°C for Cr_2Fe_2MnNi (Fig. 1a).

Table 3. EDX semi-quantitative analysis of CrFeMnNi.

% at.	Chromium	Iron	Manganese	Nickel
BCC	46.2 ± 2.0	30.3 ± 1.0	17.5 ±0.4	6.0 ± 1.4
FCC	25.0 ± 1.4	29.5 ± 2.5	26.0 ± 2.0	19.5 ± 1.7

Table 4. EDX semi-quantitative analysis of Cr_2Fe_2MnNi.

% at.	Chromium	Iron	Manganese	Nickel
BCC	47.0 ± 0.7	33.16 ± 0.5	10.9 ± 0.4	8.9 ± 0.5
FCC	28.4 ± 1.0	34.83 ± 1.5	14.8 ± 1.0	22.0 ± 1.5

For the AlCrFeMnNi-based HEAs, the DTA curves are shown in Fig. 2a. All DTA cooling curves present several peaks at high temperature, indicating the formation of complex microstructures. Indeed, almost all samples exhibit dual-phase microstructures, as shown in Fig. 3 and Fig. 4.

According to the VEC theory, the equimolar sample AlCrFeMnNi should consist in a single BCC solid solution. However, the AlCrFeMnNi sample presents a transformation that starts at 1340°C and ends at 1240°C. No further transformation occurs at lower temperatures. The detailed microstructures of this sample are illustrated in Fig. 2b and Fig. 2c. Typical dendritic and interdendritic structures were observed. The compositions of the phases in the different regions were evaluated using EDX and the results are shown in Table 5. In accordance with prior works [22,23], the dendritic region is characterized by a mixed FCC + B2 matrix rich in Cr and Fe, in which cuboid precipitates rich in Al and Ni are embedded. The interdendritic region is characterized by a BCC matrix rich in Al and Ni in which Cr-Fe rich rod-shaped B2 precipitates are embedded. The precipitates are known to form through a spinodal decomposition [22,23].
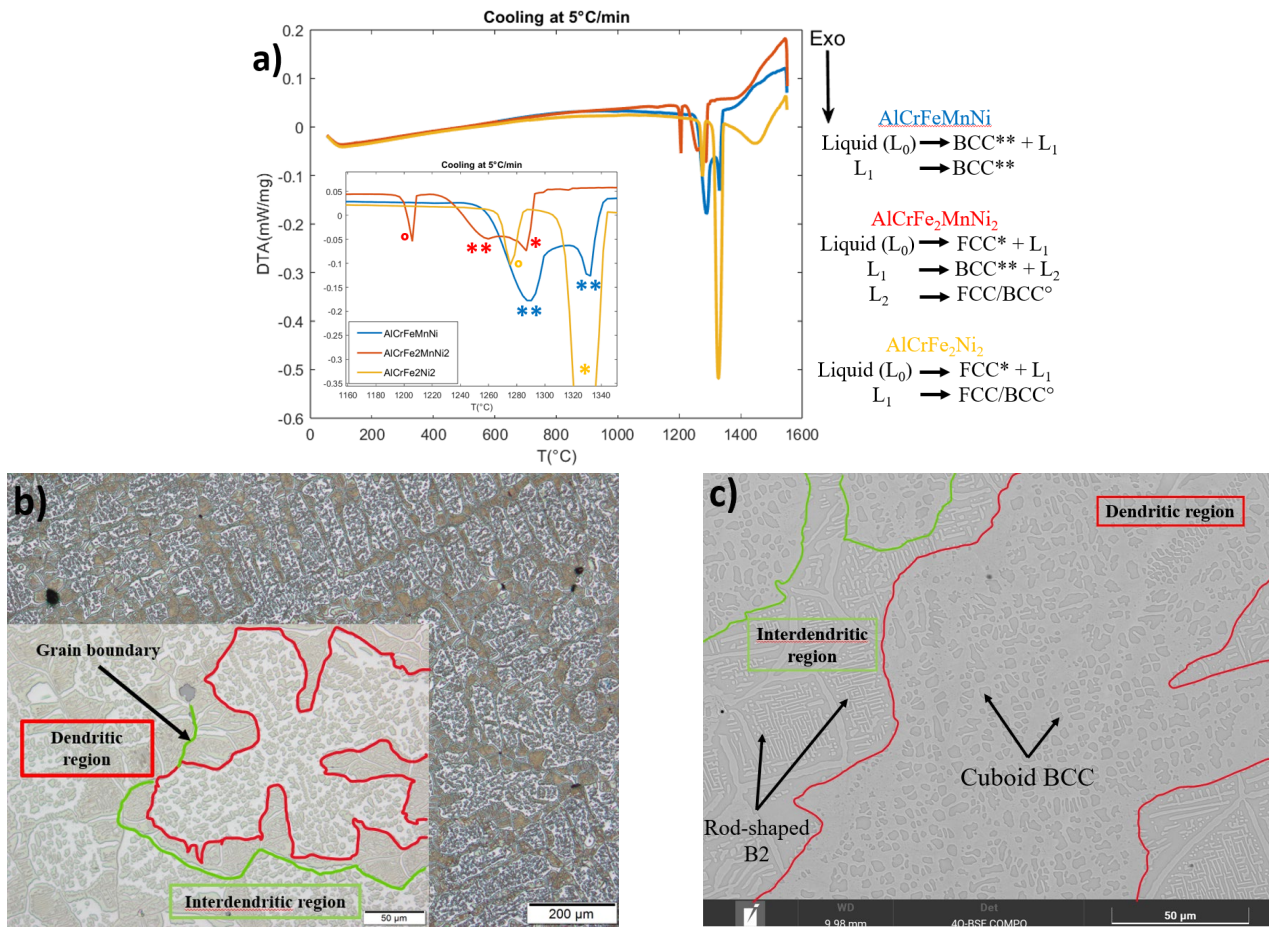
Fig. 2. (a) DTA cooling combined plots for alloys AlCrFeMnNi, AlCrFe$_2$MnNi$_2$ and AlCrFe$_2$Ni$_2$, (b) optical micrograph of alloy AlCrFeMnNi, (c) scanning electron micrograph of alloy AlCrFeMnNi.

Table 5. EDX semi-quantitative analysis of AlCrFeMnNi.

% at.	Al	Cr	Fe	Mn	Ni
Precipitates	29.4 ± 4.0	6.5 ± 3.0	9.0 ± 4.3	16.0 ± 1.5	39.1 ± 7.9
Matrix	7.7 ± 1.1	34.6 ± 1.8	30.0 ± 0.9	24.7 ± 0.5	3.1 ± 1.6

With increased amounts of Fe and Ni, the AlCrFe$_2$MnNi$_2$ sample presents a lower solidification temperature in a range between 1280°C and 1190°C (Fig. 2a). At 1210°C, the remaining liquid, which reaches the eutectic composition went through the eutectic transformation. Two different areas can be observed in the microstructure and the typical eutectic lamellar structure is present in some areas of the microstructure (Fig. 3a) [24]. This is consistent with the peaks revealed by the DTA cooling curve (Fig. 2a). Observing the SEM micrographs in Fig. 3a, the presence of the dual-phase microstructure confirms the prediction by the VEC theory for a value of 7.43 (Table 2). Compared to the equimolar AlCrFeMnNi sample, no dendritic and interdendritic regions were observed (Fig. 3a). EBSD analysis shows the presence of FCC and BCC/B2 phases (Fig. 3b). The results of EDX analysis presented in Table 6 show that the microstructure is composed by an FCC matrix rich in Fe and Cr while the BCC/B2 phase is rich with Al and Ni. The microstructure analysis suggests that a solid-state transformation corresponding to the spinodal decomposition of BCC phase into an ordered (B2) and disordered phases (BCC) occurs. The semi-quantitative

chemical analysis using EDX reveals that the elemental distribution varies between the two phases. The B2 phase is depleted in Cr and Fe compared to the BCC phase. On the other hand, Mn is nearly uniformly distributed in all the three phases present into the microstructure (Table 6).
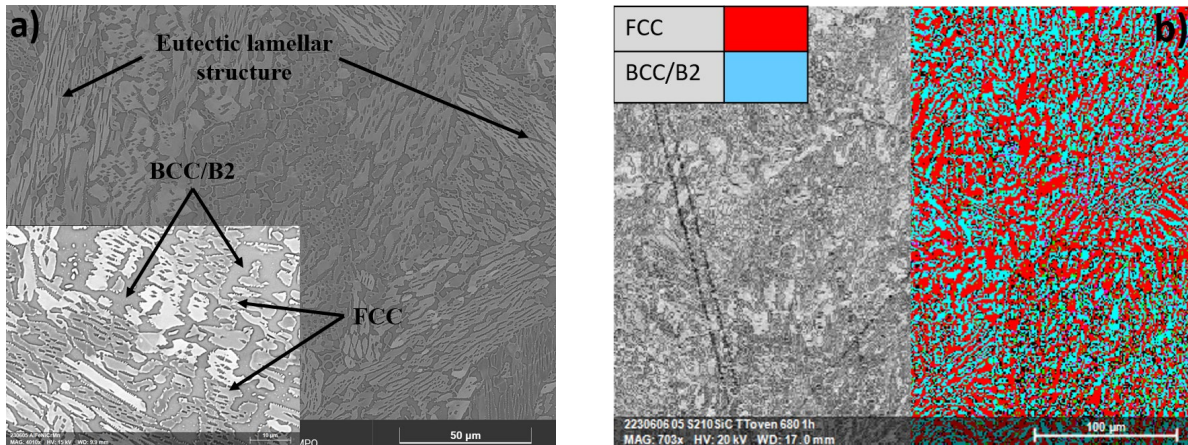

Fig. 3. (a) scanning electron micrographs of $AlCrFe_2MnNi_2$, (b) EBSD analysis of $AlCrFe_2MnNi_2$: pattern quality at left, and phase map at right.

Table 6. EDX semi-quantitative analysis of $AlCrFe_2MnNi_2$.

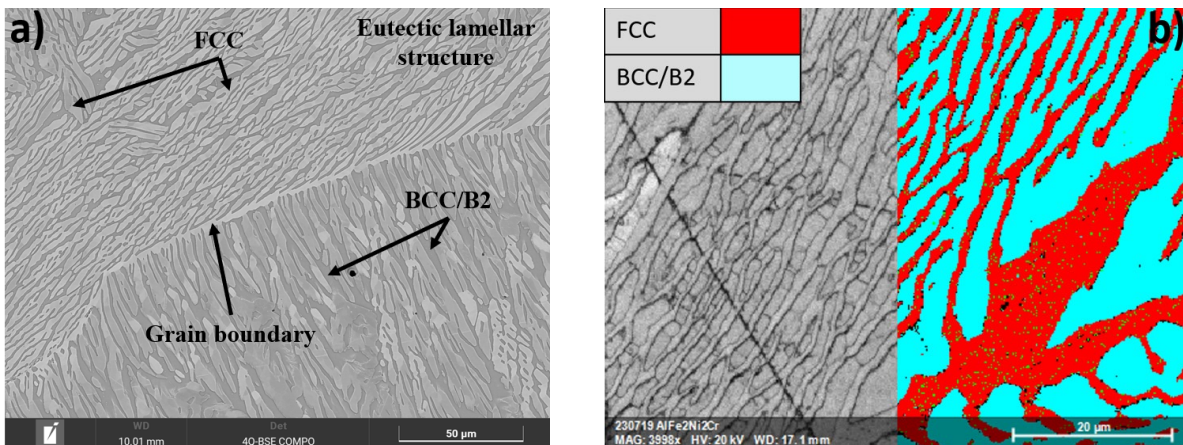| % at.	Al	Cr	Fe	Mn	Ni
FCC	4.7 ± 0.4	18.6 ± 0.9	39.6 ± 0.6	14.2 ± 0.3	22.9 ± 0.8
B2	26.0 ± 0.6	2.1 ± 0.2	7.9 ± 0.4	15.9 ± 0.5	48.1 ± 0.5
BCC	20.3 ± 5.6	10.5 ± 7.8	16.8 ± 9.0	14.0 ± 1.5	38.4 ± 9.8

Fig. 4. (a) scanning electron micrographs of $AlCrFe_2Ni_2$, (b) EBSD analysis of $AlCrFe_2Ni_2$: pattern quality at left, and phase map at right.

When the Mn is removed from the mixture, in $AlCrFe_2Ni_2$, the solidification temperature is increased up to a range between 1340°C and 1260°C (Fig. 2a). The solidification starts with the formation of the FCC phase. Around 1285°C, the remaining liquid with the eutectic composition forms the typical lamellar structure that characterize the eutectic transformation of some HEAs (Fig. 4a) [24]. The EBSD analysis revealed the presence of a dual-phase mixture composed of FCC and BCC/B2 phases (Fig. 4b). The same partitioning of elements as in $AlCrFe_2MnNi_2$ phases were found, the FCC phase is rich in Fe and Cr while BCC/B2 phase is rich in Al and Ni.

Discussion

As mentioned in the introduction, the properties of HEAs depends on the microstructure [10,11]. The VEC, that represents an important parameter for phase structures, is directly correlated to the FCC/BCC volume fraction. It is known that for high VEC, the atomic bonding forces are higher, so the atoms tend to rearrange into the FCC structure with a higher packing density, as observed in $CrFe_2MnNi_2$ sample. On the contrary, low VEC leads to lower atomic bonding forces and atoms tend to arrange into the BCC structure with lower atomic packing density [13].

In CrFeMnNi and Cr_2Fe_2MnNi samples, the microstructures present a dual-phase of FCC and BCC (Fig. 1b), which is consistent with the prediction of a dual-phase microstructure for VEC in a range between 6.8 and 8 (Table 1). The same is true for $AlCrFe_2MnNi_2$ and $AlCrFe_2Ni_2$ samples just after the end of the solidification (Table 2). The prediction theory is correctly validated. This result is significant for the field of alloy design, as it provides a foundational basis for leveraging the theory to systematically optimize microstructures according to the desired material properties.

After the solidification, at lower temperature, a solid-state transformation can occur. In fact, when Al acting as a BCC stabilizer, is added to form an equimolar AlCrFeMnNi, the microstructure should consist of a single BCC phase according to the parametric prediction theory. This theory is validated for the solidification, when solid-state transformations are not considered, because in this alloy the formation of B2 precipitates, as shown in Fig. 2c, was favored. According to the results obtained for equimolar AlCrFeMnNi in several papers [22,23], the first solid to form is BCC in both dendritic and interdendritic regions, and decreasing the temperature, the spinodal decomposition occurs. In this specific case, the spinodal decomposition is different in both regions due to the different average composition of saturated BCC phase in the two regions [22]. The solid-state transformations that occur during the cooling are not considered by the VEC theory. But it still represents a useful tool for the explanation of the HEAs microstructures, especially to predict the phases that form during the solidification. Recent works, based on the optimization of the VEC parameters, employing machine learning were able to predict a BCC+FCC+IM structure of the equimolar composition AlCrFeMnNi [25].

It is important to notice that, in near-equilibrium solidification, elements such as Mn do not actively contribute to the phase separation by preferential partitioning in AlCrFeMnNi-based HEAs. In order to design an alloy with high corrosion resistance, the distribution of the elements in both FCC and BCC phase should be taken into account. Al and Ni tend to be highly present in BCC/B2 phase while Fe and Cr are mainly present in FCC phase (Table 5 and Table 6). Knowing that the FCC phase is the preferred one for the aim of enhanced corrosion resistance, the addition of high BCC stabilizer such as Al should be carefully monitored, also due to the tendency of BCC phase containing Al to undergo further solid-state transformations and form precipitates which would reduce the corrosion resistance.

As the material response is in close relationship to the microstructure, the use of DTA to investigate and to understand the phase transformations can be a useful tool for the selection of elements and range of composition to develop an alloy that fulfill the requirements. In the case of HEAs, where the research is wide opened, DTA represents a fast experimental and cost-effective method to develop an alloy with corrosion resistance. Understanding phenomena that occur under near-equilibrium conditions, such as the significant partitioning of elements, is crucial when examining the microstructure that may arise, for instance, in the Heat Affected Zone (HAZ) of a sample produced through LPBF. Due to the high energy of the laser during the short interaction times and the high solidification rates of the melt pool, the resulting microstructure may also be strongly textured. In order to control the microstructure or to propose heat treatments to restore more homogeneous and stable microstructures, investigating the phase transformations that occur during the heating of the LPBF-printed samples through a reverse DTA is a valid option [20,21]. In addition, using the reverse DTA, the solidification path in out-of-equilibrium conditions offer

by LPBF can be fully understood. Those results are fundamental to determine the heat treatments temperatures to reach the microstructure that would fulfill the requirements.

As the next step of this work, LPBF samples will be printed with optimized parameters (laser power and scanning speed). The evolution of the microstructure from near-equilibrium to the out-of-equilibrium conditions brought by the ultra-fast cooling in LPBF, will be investigated.

Summary

The VEC theory is a useful tool to predict the first phases that form during the solidification in HEAs as either FCC, BCC, or mixture of both phases, but does not consider solid-state transformations. In particular, in Cr, Fe, Mn, Ni system, the addition of Al promotes the formation of BCC phase followed by its spinodal decomposition. In AlCrFeMnNi-based HEAs, FCC phase is rich in Fe and Cr while BCC phase is Al-Ni rich, and Mn is equally distributed in all phases. In absence of Al, the Mn tend to partition mainly in FCC phase as observed in CrFeMnNi and Cr_2Fe_2MnNi.

DTA analysis represents a rapid and cost-effective test to investigate transformations that occur during heating and cooling in near-equilibrium conditions. These results can then be used as reference to understand the mechanisms and phenomena that occur in out-of-equilibrium conditions and to guide the design of new alloys and/or thermal treatments.

References

[1] I. Ribeiro, F. Matos, C. Jacinto, H. Salman, G. Cardeal, H. Carvalho, R. Godina, P. Peças, Framework for life cycle sustainability assessment of additive manufacturing, Sustainability, 12 (2020) 929. https://doi.org/10.3390/su12030929

[2] T.T. Wohlers, Wohlers report 2010: additive manufacturing state of the industry annual worldwide progress report, Wohlers Associates, 2010.

[3] F. Bartolomeu, M. Gasik, F.S. Silva, G. Miranda, Mechanical Properties of Ti6Al4V Fabricated by Laser Powder Bed Fusion: A Review Focused on the Processing and Microstructural Parameters Influence on the Final Properties, Metals 12 (2022) 986. https://doi.org/10.3390/met12060986

[4] M.N. Dogu, E. McCarthy, R. McCann, V. Mahato, A. Caputo, I.U. Ahad, D. Brabazon, Digitisation of metal AM for part microstructure and property control, Int. J. Mater. Form. 15, 30 (2022). https://doi.org/10.1007/s12289-022-01686-4

[5] W.E. King, A.T. Anderson, R.M. Ferencz, N.E. Hodge, C. Kamath, S.A. Khairallah, A.M. Rubenchik, Laser powder bed fusion additive manufacturing of metals: physics, computational, and materials challenges, Appl. Phys. Rev. 2. (2015). https://doi.org/10.1063/1.4937809

[6] S. Chowdhury, N. Yadaiah, C. Prakash, S. Ramakrishna, S. Dixit, L.R. Gupta, D. Buddhi, Laser powder bed fusion: a state-of-the-art review of the technology, materials, properties & defects, and numerical modelling, J. Mater. Res. Technol. 20 (2022) 2109-2172

[7] R. Pal, A. Basak, Linking powder properties, printing parameters, post-processing methods, and fatigue properties in additive manufacturing of AlSi10Mg, Alloys 1 (2022) 149-179.

[8] J.W. Yeh, S.K. Chen, S.J. Lin, J.Y. Gan, T.S. Chin, T.T. Shun, S.H. Tsau, S.Y. Chang, Nanostructured high-entropy alloys with multiple principal elements: novel alloy design concepts and outcomes, Adv. Eng. Mater. 6 (2004) 299–303. https://doi.org/10.1002/adem.200300567

[9] B. Cantor, I.T.H. Chang, P. Knight, A.J.B. Vincent, Microstructural development in equiatomic multicomponent alloys, Mater. Sci. Eng. 375–377 (2004) 213–218.

[10] Y. Zhang, T.T. Zuo, Z. Tang, M.C. Gao, K.A. Dahmen, P.K. Liaw, Z.P. Lu, Microstructures and properties of high-entropy alloys, Prog. Mater Sci. 61 (2014) 1–93.

[11] S. Guo, C. Ng, J. Lu, C.T. Liu, Effect of valence electron concentration on stability of fcc or bcc phase in high entropy alloys, J Appl Phys. 109. (2011).

[12] D.B. Miracle, O.N. Senkov, A critical review of high entropy alloys and related concepts, Acta Mater. 122 (2017) 448–511. https://doi.org/10.1016/j.actamat.2016.08.081

[13] W. Zhang, A. Chabok, B.J. Kooi, Y. Pei, Y., Additive manufactured high entropy alloys: A review of the microstructure and properties, Mater. Des., 220 (2022) 110875. https://doi.org/10.1016/j.matdes.2022.110875

[14] X. Yang, Y. Zhang, Prediction of high-entropy stabilized solid-solution in multi-component alloys, Mater. Chem. Phys. 132 (2012) 233–238.

[15] B.S. Li, Y.P. Wang, M.X. Ren, C. Yang, H.Z. Fu, Effects of Mn, Ti and V on the microstructure and properties of AlCrFeCoNiCu high entropy alloy, Mater. Sci. Eng. 498 (2008) 482-486. https://doi.org/10.1016/j.msea.2008.08.025

[16] A. Inoue, B. Shen, A. Takeuchi, Developments and applications of bulk glassy alloys in late transition metal base system, Mater. Trans. 47 (2006) 1275-1285.

[17] Y. Shi, B. Yang, P.K. Liaw, Corrosion-resistant high-entropy alloys: A review, Metals 7 (2017). https://doi.org/10.3390/met7020043.

[18] J. Tamminen, Thermal analysis for investigation of solidification mechanisms in metals and alloys, Dept. of Structural Chemistry, University of Stockholm, Sweden. (1988).

[19] D.M. Stefanescu, Thermal analysis-theory and applications in metalcasting, Int. J. Met. 9. (2015). https://doi.org/10.1007/BF03355598

[20] T. Maurizi Enrici, O. Dedry, F. Boschini, J.T. Tchuindjang, A. Mertens, Microstructural and Thermal Characterization of 316L + WC Composite Coatings Obtained by Laser Cladding, Adv. Eng. Mater. 22. (2020). https://doi.org/10.1002/adem.202000291

[21] T. Maurizi Enrici, A. Mertens, M. Sinnaeve, J.T. Tchuindjang, Elucidation of the solidification sequence of a complex graphitic HSS alloy under a combined approach of DTA and EBSD analyses, J. Therm. Anal. Calorim. 141 (2020) 1075–1089. https://doi.org/10.1007/s10973-019-09093-9

[22] A. Munitz, L. Meshi, M.J. Kaufman, Heat treatments' effects on the microstructure and mechanical properties of an equiatomic Al-Cr-Fe-Mn-Ni high entropy alloy, Mater. Sci. Eng. 689 (2017) 384–394. https://doi.org/10.1016/j.msea.2017.02.072

[23] E. Ananiadis, K. Lentzaris, E. Georgatis, C. Mathiou, A. Poulia, A.E. Karantzalis, AlNiCrFeMn equiatomic high entropy alloy: a further insight in its microstructural evolution, mechanical and surface degradation response, Met. Mater. Int. 26 (2020) 793–811.

[24] Y. Lu, Y. Dong, S. Guo, L. Jiang, H. Kang, T. Wang, B. Wen, Z. Wang, J. Jie, Z. Cao, H. Ruan, T. Li, A promising new class of high-temperature alloys: Eutectic high-entropy alloys, Sci. Rep. 4. (2014). https://doi.org/10.1038/srep06200

[25] A. Oñate, J.P. Sanhueza, D. Zegpi, V. Tuninetti, J. Ramirez, C. Medina, M. Melendrez, D. Rojas, Supervised machine learning-based multi-class phase prediction in high-entropy alloys using robust databases, J. Alloys Compd. 962 (2023) 171224. https://doi.org/10.1016/j.jallcom.2023.171224